Journal of Alloys and Compounds 601 (2014) 167–174

Contents lists available at ScienceDirect

Journal of Alloys and Compounds

journal homepage: www.elsevier.com/locate/jalcom

In situ gas bubble-assisted one-step synthesis of polymorphic Co_3O_4 nanostructures with improved electrochemical performance for lithium ion batteries

Guoxiu Tong [a,*], Yun Liu [a], Jianguo Guan [b,*]

[a] College of Chemistry and Life Sciences, Zhejiang Normal University, Jinhua 321004, PR China
[b] State Key Laboratory of Advanced Technology for Materials Synthesis and Processing, Wuhan University of Technology, Wuhan 430070, PR China

ARTICLE INFO

Article history:
Received 17 November 2013
Received in revised form 21 February 2014
Accepted 24 February 2014
Available online 5 March 2014

Keywords:
Co_3O_4 nanobowl arrays
Nanotube arrays
Gas bubble-induced self assembly
Electrochemical activity

ABSTRACT

A novel and versatile gas bubble-assisted self-assembly technique was developed for the first-time preparation of Co_3O_4 nanobowl arrays by the rapid thermal decomposition of $Co(NO_3)_2{\cdot}6H_2O$ on a flat substrate. The morphological modulation from novel nanobowl arrays, to nanotube arrays, to nanorods, and even to microspheres can be realized by only tuning decomposition temperature from 150 °C to 700 °C. The in situ generated (O_2, H_2O, NO_2) bubbles guided the growth of Co_3O_4 nuclei, resulting in the final morphology of Co_3O_4 nanostructures. The Co_3O_4 nanostructures were characterized by X-ray diffraction, Fourier-transform infrared spectroscopy, scanning electron microscopy, transmission electron microscopy, and nitrogen adsorption–desorption isotherms. Analysis of electrochemical properties revealed that Co_3O_4 nanobowl and nanotube arrays obtained at low temperatures displayed significant enhancement of electrochemical activity because of low crystallization, small grain size, high specific surface area, and hierarchically porous structure. This simple process was applicable to large-scale production and may be extended to other materials. The porous/hollow structure and high specific surface area of the as-obtained Co_3O_4 nanobowl and nanotube arrays can enable their potential use in catalysis, chemical sensing, luminescence, energy storage, controlled release, and cellular applications.

1. Introduction

The preparation of bowl-shaped micro/nanostructures has been the subject of many recent publications in the field of material science. These bowl-shaped structures play a pivotal role in a wide range of industrial and biological applications involving biomedical and nanofluidic devices [1], nanosphere selection [2], coercivity enhancement [3], and photocatalysis [4]. Strategies for synthesizing bowl-shaped containers, such as milling-etching method, nanosphere lithography and sputtering technique, monolayer self-assembly and electroforming approach, and chemical polymerization, have been extensively reported. Various bowl-shaped micro/nanostructures, including polymer [5], metal oxide (ZnO [6], TiO_2 [7], CuO [8]), and metal (Pt [9], Ni [10], Co [1], Au [11]) have been successfully obtained. However, the above techniques for preparing bowl-shaped microstructures are mainly based on template strategy, that is, the following three steps are generally involved. One is to synthesize such hard templates as polystyrene nanosphere (PS), silica, poly-(vinyl alcohol) nanowell arrays, and PS-b-PEO diblock copolymer. Second is the formation of the nanoshells by different coating techniques (e.g., reduction, evaporating/sputtering deposition, electrochemical deposition, and solution/sol dipping deposition). The last one is the removal of the templates through annealing, dissolving, etching, or deep UV irradiation. In addition, as for the milling–etching technique, ion milling was also used to remove the top half of core–shell spheres. Apparently, the aforesaid template-assisted procedures suffer a number of limitations, such as complicated multi-step, especial experiment setup, and high cost, which restrict their practical applications to some extent. The development of facile, low cost, and effective strategies for synthesizing bowl-shaped structures, therefore, is urgently expected in potential applications of shape-dependent property devices.

Polymorphous Co_3O_4 nanostructures have attracted considerable attention because of their potential applications in many different scientific and technological fields [12–15]. As properties of Co_3O_4 nanostructures greatly depend on their shape, Co_3O_4 nanostructures of various morphologies have been prepared, including nanocubes [16] hollow spheres [17], nanorods [18], nanowires

---

* Corresponding authors. Tel.: +86 15167953171.
E-mail addresses: tonggx@zjnu.cn, wwhtgs@126.com (G. Tong), guanjg@whut.edu.cn (J. Guan).

http://dx.doi.org/10.1016/j.jallcom.2014.02.152
0925-8388/

[19,20], nanotubes [21,22], nanowalls [23], and nanoflowers [24]. Among the rich nanostructural morphologies revealed by Co_3O_4, the nanobowl is never seen, but such unusual structures represent an interesting platform for various applications in optical, electronic, and biomimetic fields.

The gaseous bubble/gas flow-assisted synthesis strategy, a simple template-free technique, has the potential to construct organic and/or inorganic materials into micro/nanostructures with a range of well-defined morphologies on a large scale [25–27]. The aforesaid synthesis strategy has aroused much popular interest for its simplicity, high efficiency, and low cost, which can overcome the disadvantages of the hard template. In particular, morphological modulation can be easily achieved through kinetically controlling the number, distribution, size, and self-assembly behavior of gas bubbles in the dispersion system. Successful synthesis of some particular micro/nanostructures had been achieved, including polypyrrole microcontainers (bowls, cups, goblets, and bottles) [28–31], polymer microstructure [32], Co hollow mesospheres [33], and Fe nanocircle [34]. We have deeply studied the assembly behavior of gas flow in CVD and gas bubbles in solution. We reported that Fe nanofibers could form under the impact of the carrier gas flow and the spontaneous magnetization of magnetic nanoparticles [35]. Moreover, using H_2 gas bubbles in situ generated in the liquid reduction reaction to direct the assembly of Fe nuclei can generate polymorphic nanostructures, including nanofibers, nanotubes, and hollow nanospheres [36]. Additionally, this strategy was expanded to solid phase synthesis. We found that the thermal decomposition of inorganic salt (e.g., nitrate salt) also released a large number of gas bubbles or gas, which could serve as template to induce the assembly and growth of flower-like structures [37] and nanotube arrays [38].

We further developed the above gas bubble-assisted assembly method for the first time preparation of Co_3O_4 nanobowl arrays. Decomposition temperature (T_d), as a key kinetic factor, was used to modulate the structure and morphology of the resultant Co_3O_4 nanostructures. The electrochemical properties of the obtained polymorphous Co_3O_4 nanostructures were investigated in detail.

2. Experimental section

2.1. Chemicals

All reagents of analytical grade were obtained from Shanghai Chemical Reagent Co. Ltd. in China and used without any further purification.

2.2. Preparation of nanobowl arrays

In a typical synthesis, a stainless steel substrate with 4.0 cm × 4.0 cm × 3.0 mm in size was placed on a flat-heater (IKA C-MAG HS7) and was heated to 150 °C at a heating-up rate of 10 °C min^{-1}. Then, 2.97 g $Co(NO_3)_2 \cdot 6H_2O$ solid powders were uniformly spread onto the substrate at once and kept at T_d = 150 °C for 5 h. A black film, which was easily peeled out of the substrate, was obtained by naturally cooling to room temperature with the flat-heater, washing with dieonized water and absolute ethanol for several times to remove unexpected impurities, and finally drying in a vacuum oven at 80 °C for 5 h. The reaction process was carried out within a mantle with an outlet to let the generated gases out to a 1.0 M sodium hydroxide solution through a rubber pipe. Morphological modulation was achieved by changing T_d. For example, thermally decomposing $Co(NO_3)_2 \cdot 6H_2O$ at T_d = 200 °C for 1 h can generate the contorted, tube-like nanostructures and at T_d = 300–400 °C for 1 h can form nanotube arrays.

2.3. Preparation of nanorods and microspheres

Unlike preparing nanotube arrays, $Co(NO_3)_2 \cdot 6H_2O$ described above was uniformly spread into a ceramic vessel (1.2 cm × 9.0 cm × 1.0 cm) and immediately placed in a horizontal tube furnace after the furnace temperature has been elevated to the designated value (i.e., 500 °C for nanorods and 700 °C for microspheres). The above vessel was kept at the designated temperature for 1 h. Other procedures were the same with preparation of nanobowl arrays.

2.4. Sample characterization

The morphologies, chemical composition, and crystalline structure of the as-prepared samples were studied by X-ray diffraction (XRD, D/MAX-IIIA, Cu Kα radiation, $\lambda = 0.15406$ nm,10 deg /min), Fourier-transform infrared (FTIR, Nicolet FTIR-170SX, 4000–400 cm^{-1}, room temperature) absorption spectra, field-emission scanning electron microscopy (FE-SEM, Hitachi S-4800, 10 kV), and transmission electron microscopy (HRTEM, JEM-2100F, 200 kV).

Nitrogen adsorption–desorption isotherms were obtained on a nitrogen adsorption apparatus (ASAP 2020 M Micromeritics instruments, USA). The samples are degassed at 150 °C prior to Brunauer–Emmett–Teller (BET) measurements. The BET specific surface area (S_{BET}) is determined by a multipoint BET method using the adsorption data in the relative pressure P/P_0 range of 0.05–0.25. The pore size distribution derived from the desorption isotherm using the Barret–Joyner–Halender method. The nitrogen adsorption volume at a P/P_0 of 0.995 was used to determine the pore volume and porosity.

2.5. Measurement of electrochemical properties

Electrochemical measurements were carried out using two-electrode cells with lithium metal as the counter and reference electrodes. The working electrode was fabricated by compressing a mixture of the active Co_3O_4 materials, conductive material (acetylene black, ATB), and binder (polytetrafluoroethylene, PTFE) in a weight ratio of Co_3O_4/ATB/PTFE = 70:30:10. The battery assembly was performed in a glove-box filled with pure argon, in which the negative piece, Celgard2400 membrane, and lithium chip were sandwiched, and an appropriate amount of electrolyte was added before sealing. The newly installed battery was measured by a discharge–charge method on a model Land CT2001A multichannel battery tester in the potential range of 0–3.0 V, at current densities of 35–70 mA g^{-1} and at 20 °C after hold for 4 h.

3. Results and discussion

3.1. Phase and structure characterizations

To clarify the structure of the products obtained at different T_d, XRD and IR tests were carried out. Fig. 1A presented the XRD

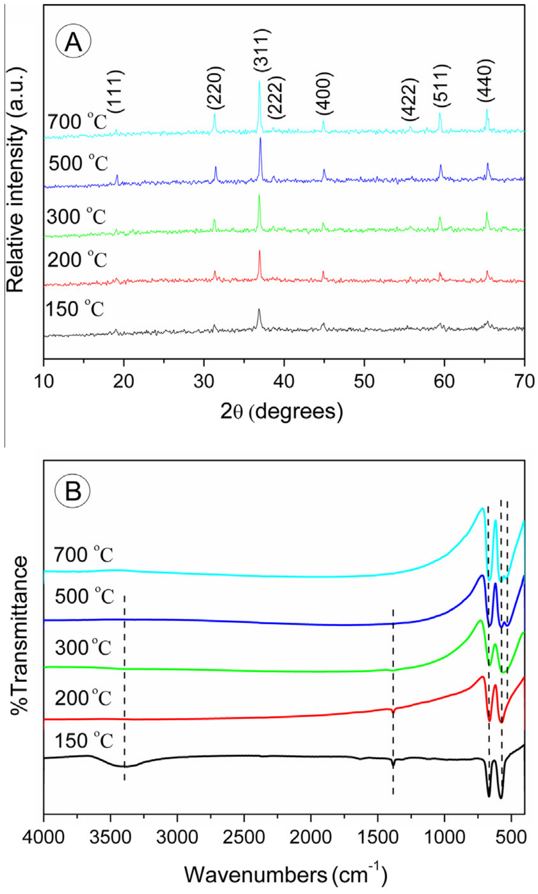

Fig. 1. XRD patterns (A) and IR spectra (B) of the products obtained at different T_d.

patterns of the samples, in which all diffraction peaks possessed the same position but different intensities. As for the samples formed at 150 °C, these diffraction peaks at 10–90° can be indexed to the face centered cubic Co_3O_4, space group *Fd3m* with the lattice parameter $a = 0.8056$ nm (JCPDS Card No. 65-3103). Co_3O_4 then began to appear at the relatively low temperature of 150 °C for 5 h, which is in good agreement with the literature [39]. Meanwhile, low intensity peaks from the above samples suggest low crystallization and defect existence. Owing to the enhancement of crystallization and crystallite size, a further increase in T_d from 200 °C to 700 °C gradually strengthened the diffraction peaks. The mean crystallite size (δ) and strain (ε) data of all the as-obtained samples were calculated by the Hall–Williamson equation and listed in Table 1. The δ values increased from 11.1 nm to 67.1 nm and the ε decreased from 0.510% to 0.108% when T_d varied from 150 °C to 700 °C.

To further verify the results, the products formed at $T_d = 150$ °C to 700 °C underwent FT-IR analysis. The IR absorption peaks centered at ca. 666 and 575 cm^{-1} (Fig. 1B) confirmed the formation of spinel Co_3O_4 [40–42]. The aforementioned peak intensity increased with T_d, hinting Co_3O_4 crystallization enhancement [36,43]. The peaks at 3431 and 1640 cm^{-1} were assigned to the O—H stretching and bending modes of physical-absorption water or hydroxide [44], respectively. The sharp peak at 1384 cm^{-1} came from ν3 vibration of NO_3^- [45], indicating the existence of minor intermediate products. Owing to the thorough conversion of minor intermediate products to Co_3O_4, the peaks located at 3431, 1640, and 1384 cm^{-1} completely disappeared when T_d was further elevated. The above data demonstrate that the crystallization and grain size of the products can easily be modulated by changing the T_d. Apparently, the products formed at the relatively low T_d had low crystallization and small grain size, exhibiting distinct and novel electrochemical properties because of a quantum and surface effect.

3.2. Morphology observation

Further insight into the morphology and microstructure of the Co_3O_4 products was gained using SEM and TEM. Fig. 2A showed that many Co_3O_4 nanobowls were uniformly arrayed on the substrate in high densities of 5×10^5 units mm^{-2} to 6×10^5 units mm^{-2} while decomposing $Co(NO_3)_2{\cdot}6H_2O$ at 150 °C. Gradually magnified SEM images in Figs. 2B and C revealed that these nanobowls were a square with sides of 1.5–2.0 μm and wall thicknesses of 100–200 nm, as well as smooth surface. Otherwise, circular nanobowls with 80 ± 20 nm in diameter, 20 ± 5 nm in wall thickness, and 25 ± 5 nm in depth can also be observed (Figs. 2D–2F). The enlarged TEM images from the edge of a nanobowl (Fig. 2G) showed that the nanobowls consisted of uniform and tiny nanoparticles of 10–20 nm in size. The FFT of the entire region in Fig. 2G was carried out and the pattern was shown in Fig. 2H. The indexed, clear, diffused rings in the SAED pattern suggest that the nanobowls were polycrystalline.

Table 1
Effect of decomposing temperature (T_d) on mean crystallite size (δ), strain (ε), BET specific surface area (S_{BET}), pore volume (V), and pore size (D) of the Co_3O_4 nanostructures.

T °C	Shape	δ nm	ε %	Textural characteristics		
				S_{BET} m^2 g^{-1}	V cm^3 g^{-1}	D nm
150	Nanobowl	11.1	0.510	66.31	0.061	3.70
200	Contorted nanotube	13.7	0.429	63.01	0.18	11.20
300	Nanotube array	15.9	0.253	41.72	0.12	11.32
500	Nanorod	48.2	0.148	0.65	0.00076	4.65
700	Microsphere	67.1	0.108	/	/	/

No nanobowls but contorted, tube-like Co_3O_4 nanostructures were found at $T_d = 200$ °C (Figs. 3A–C). When the T_d varied from 300 and 400 °C, the products were a vertically aligned array of nanotubes with an open end (Fig. 3E). All nanotubes had a relatively uniform length up to approximately 300 nm, with one end freestanding and the other end merged into a film (Fig. 3D). The nanotubes were 50–60 nm in outer diameter, with a wall thickness of 10 nm and a relatively rough surface feature (Fig. 3F).

By further elevating T_d to 500 °C, only a mass of solid nanorods 30 ± 5 nm in diameter and 50 nm to 200 nm in length could be observed (Figs. 4A and B). More interestingly, numerous spherical congregations 2.0 μm to 3.0 μm in size composed by the nanorods were formed if the decomposition of $Co(NO_3)_2{\cdot}6H_2O$ powders was carried out at 700 °C (Figs. 4C and D). This result indicates that a hollow/porous structure with low crystallization and small grain size was easily formed at the relatively low T_d, conversely, and the solid rods and spheres with high crystallization and large grain size were produced.

3.3. Formation mechanism

Formation of bowl-shaped micro/nanostructures is mainly dependent on template strategy. Obviously, no templates or surfactants were introduced to the current reaction system. Based on the aforementioned data, therefore, we proposed a simple gas bubble-induced self-assembly technique for the novel one-step preparation of polymorphous Co_3O_4 nanostructures, as depicted in Fig. 5. Such nanostructures were synthesized by uniformly spreading $Co(NO_3)_2{\cdot}6H_2O$ solid powders on a flat stainless steel substrate and heating at various T_d. The pink powders were first melted and then turned into a black film covering the substrate. During the process, several major steps were involved: (1) $Co(NO_3)_2{\cdot}6H_2O$ grains (Fig. 5A) quickly melted into a thin liquid membrane, which covers the substrate, because of a low melting point of only 55 °C (Fig. 5B); and (2) Thermal decomposition of $Co(NO_3)_2{\cdot}6H_2O$ occurred in terms of the following chemical reaction:

$$3Co(NO_3)_2 \cdot 6H_2O \xrightarrow{\Delta} Co_3O_4 + O_2\uparrow + 6NO_2\uparrow + 18H_2O\uparrow \qquad (1)$$

Obviously, the products were Co_3O_4 nuclei in combination with a large amount of gas bubbles, including O_2, NO_2, and water vapor (Fig. 5C).

(3) Gas bubbles induced the self assembly and growth of Co_3O_4 nanostructures. According to our previous work, some important factors, including the viscosity of the carrier solution, number, size, and transport rate of the gas bubbles, and the growth rate of the nuclei, all strongly influence the gas bubble-induced assembly behavior of nuclei. These factors can be tuned by changing the reaction time, temperature, and even air pressure [37,38]. In the current study, T_d affected the gas bubble-induced self assembly of Co_3O_4 nanostructures in the following two aspects. One, T_d provided a driving force for the decomposition of $Co(NO_3)_2{\cdot}6H_2O$ and the nucleation and growth of Co_3O_4. The T_d determined the decomposition velocity of $Co(NO_3)_2{\cdot}6H_2O$. The higher T_d, the more quickly $Co(NO_3)_2{\cdot}6H_2O$ decomposed and the more Co_3O_4 nuclei and bubbles in situ generated at per unit time. Therefore, higher T_d favored the nucleation and growth of Co_3O_4, as well as the generation of gas bubbles. The other, T_d adjusted the viscosity of molten $Co(NO_3)_2{\cdot}6H_2O$ and the diffusion rate/assembly behavior of the gas bubbles, as well as the evaporation rate of crystal water. In general, the higher T_d, the higher evaporation rate of crystal water, and the lower viscosity of $Co(NO_3)_2{\cdot}6H_2O$ solution phase [46,47]. In such cases, bubbles can carry Co_3O_4 nuclei to rapidly move up in the solution and then were easily separated from Co_3O_4 nuclei

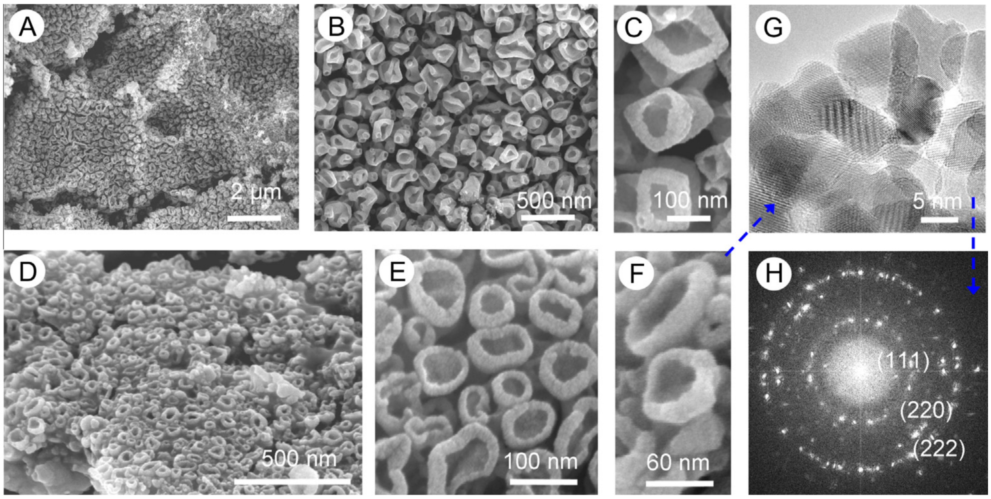

Fig. 2. Low- and high-magnification SEM images of (A–C) quadrate and (D–F) circular Co_3O_4 nanobowl arrays obtained via decomposing $Co(NO_3)_2{\cdot}6H_2O$ at 150 °C. (G) HRTEM image of the region highlighted by the square in (F). (H) Corresponding fast Fourier translation (FFT) pattern of the (G).

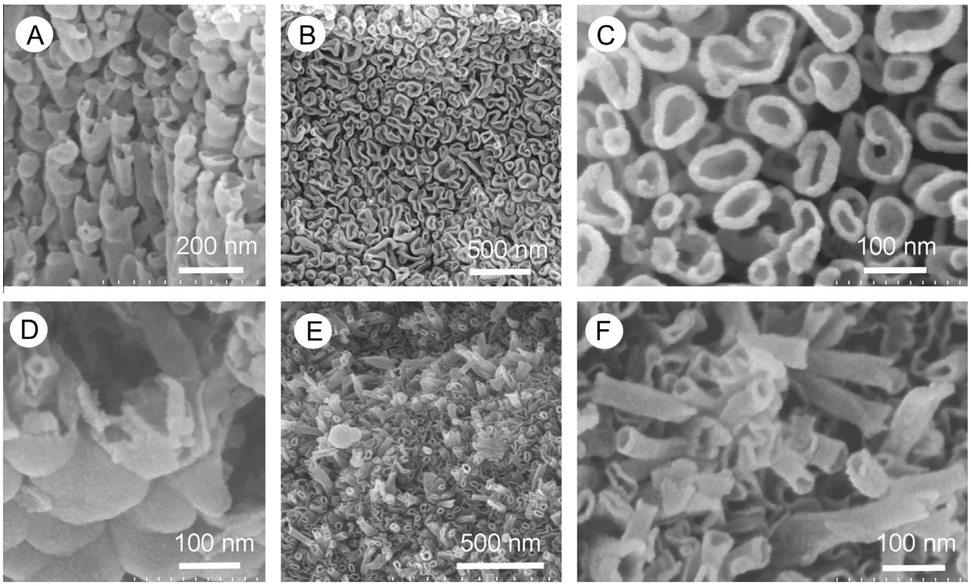

Fig. 3. Tilted side view (A), top view (B), and high-magnification FE-SEM images of the top (C) of contorted, tube-like Co_3O_4 nanostructures formed via thermal decomposition of $Co(NO_3)_2{\cdot}6H_2O$ on Fe foil at 200 °C. Bottom view (D), top view (E), and magnified SEM image of the arrayed Co_3O_4 nanotubes formed at 300 °C.

and the reaction system. All these details play critical roles in the morphological evolution of the Co_3O_4 nanostructures.

At the low T_d (i.e., 150 °C to 400 °C), these bubbles carry the Co_3O_4 nuclei to the solution surface to form a Co_3O_4 thin film (Fig. 5C1). Herein, the formation of nanobowls at T_d = 150 °C may be caused by the low decomposition velocity and the high viscosity. The former caused the decreased number of gas bubbles, and the latter hindered the transport and separation of gas bubbles in/from the solution. In this case, small amounts of gas bubbles were slowly produced and suspended on the surface of the film. These bubbles acted as template to guide the self assembly of Co_3O_4 nuclei and finally broke down (Fig. 5D1) to form nanobowls (Fig. 5E1).

As the T_d increased to 200 °C, the increased number of generated gas bubbles resulted in the higher pressure inside the film than outside. Afterward, the gas bubbles carried Co_3O_4 nuclei to slowly move up and broke through the Co_3O_4 thin film, forming protrusion crevasses or holes (Fig. 5D2). The relatively low decomposition velocity and high viscosity hindered the transport and separation of the bubbles in/from the solution, therefore forming the intermittent column-like gas flow. These ruleless gas flows acted as the template and assisted the Co_3O_4 nuclei to assemble into the contorted tube-like nanostructures.

By contrast, the growth of nanotube arrays at T_d = 300–400 °C may be ascribed to the increased decomposition velocity and decreased viscosity. In this case, a lot of gas bubbles were generated at a high diffusion rate. These bubbles rapidly moved up and passed through the Co_3O_4 thin film. As a result, protrusion crevasses or holes appeared because of the increased pressure (Fig. 5D2). Subsequently, nanotubes grew at the edge of the holes via the assembly of Co_3O_4 nuclei carried by gas bubbles, eventually forming vertically aligned arrays of Co_3O_4 nanotubes (Fig. 5E2).

At the relatively high T_d (e.g., 500 and 700 °C), the high reaction rate of molten $Co(NO_3)_2{\cdot}6H_2O$ increased the diffusion/aggregation rate of gas bubbles. In particular, the high evaporation rate of crystal water led to the rapid conversion of the reaction system

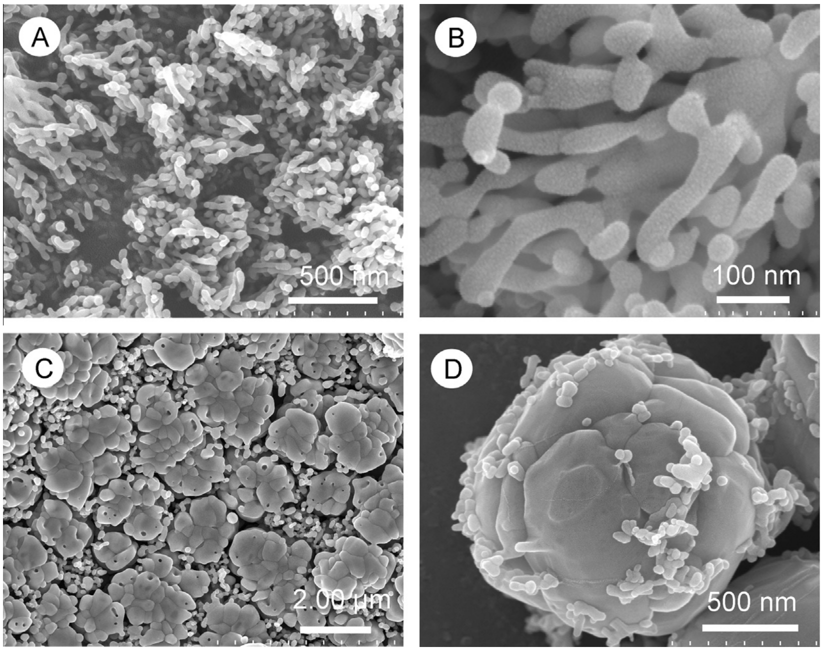

Fig. 4. Low- and high-solution SEM images of (A and B) Co_3O_4 nanorods formed at 500 °C and (C and D) Co_3O_4 microspheres produced at 700 °C.

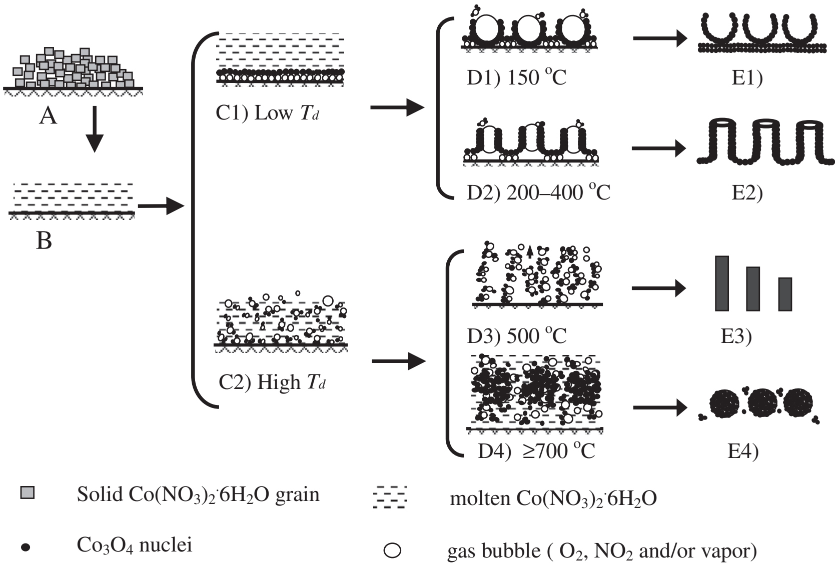

Fig. 5. Schematic illustration of the experimental procedure that generates Co_3O_4 nanobowls, nanotubes, nanorods, and microspheres: (A) $Co(NO_3)_2{\cdot}6H_2O$ grains added to the base were heated and formed molten state (B); (C1 and C2) Co_3O_4 nucleus generation through decomposing $Co(NO_3)_2{\cdot}6H_2O$ at various temperatures; (D1–D4) Co_3O_4 nucleus assembly into the polymorphous nanostructures guided by the in situ generated gas bubbles (including O_2, NO_2, and/or vapor) under different temperatures; (E1–E4) Formation of Co_3O_4 nanostructure arrays with final morphologies ranging from microspheres, to nanotubes, nanorods, and nanobowls.

from liquid phase to solid phase. Obviously, the reaction system of liquid phase is fit for the gas bubble-induced self-assembly strategy, so this strategy will lose effectiveness in the high T_d. Under this condition, the continuous gas flow was formed at T_d = 500 °C, which directed the assembly of Co_3O_4 nuclei into solid nanorods. Meanwhile, the relatively high T_d also provided a powerful driving force for the nanocrystal growth. These nanocrystals grew up by the fusion of Co_3O_4 nuclei or nanoparticles, causing the shrinkage and even disappearance of the pore size with increased T_d. Therefore, the growth of microspheres produced at T_d = 700 °C was ascribed to the high nucleation and growth rate rather than the induction role of gas bubbles. The above results indicate that changing T_d can effectively tailor the shape and structure of the as-made products.

In addition, heating rate is also a key factor for forming nanostructures. We found a high heating rate favored the formation of nanobowls, nanotubes, and nanorods. On the contrary, if the samples were slowly heated up to higher temperature, only spherical aggregates were obtained. This may be because the slow heating process leads to the evaporation of a mass of crystal water. In the absence of crystal water, the gas bubble-induced self-assembly technique no longer worked. This further verified the hypothesis of the gas bubble-induced self-assembly strategy proposed above. So we selected to directly spread $Co(NO_3)_2{\cdot}6H_2O$ onto the heated substrate.

Our method has several important advantages over other technologies. Our approach is more simple, convenient, and efficient; the differences involved are as follows: Above all, a rapid thermal decomposition route based on only a common cobalt nitrate salt, without the addition of any chemical reagents (including the surfactant, even the solvent), is used instead of the solution phase reaction. Moreover, the gas bubbles with high speed are generated in situ in the thermal decomposition reaction other than those released from the additional reaction (e.g., the electrolysis process of H_2O or the decomposition of hydrogen peroxide [21]). Last but not the least, various kinetic factors, such as thermal decomposition temperature and pressure, were applied to modulate the size, number, and release speed of the gas bubbles and therefore easily tuned the final morphology of the resulting products. Our novel approach is hopefully extended to synthesize hollow metal and/or metal oxide nanotubes or nanotube arrays on various substrates.

3.4. Textural characteristics

Aside from the modulation of crystallinity, grain size, and morphology, the T_d also contributed significantly to the textural properties of the products. The textural properties of the Co_3O_4 products were further characterized by measuring nitrogen physical adsorption/desorption isotherms, as shown in Fig. 6. The products formed at 150 °C to 300 °C showed the type IV isotherms (Fig. 6A). With T_d gradually increased to 300 °C, the curves were distinctly split into two separate hysteresis loops, indicating the appearance of the bimodal pore-size distributions. The hysteresis features of Co_3O_4 products at a low relative pressure ($0.4 < P/P_0 < 0.75$) should be classified as type H2 loop, suggesting the presence of ink-bottle pore. In contrast, these hysteresis loops at a high relative pressure ($0.75 < P/P_0 < 1.0$) were of type H3, corresponding to slit-shaped pores from aggregates of plate-like particles. The bimodal pore-size distribution was further confirmed by the corresponding pore-size distribution of the Co_3O_4 products (Fig. 6B). As shown in the pore distribution curves of Fig. 6B, the Co_3O_4 nanobowl and nanotube arrays produced at the low T_d of 150 °C to 300 °C had a bimodal pore distribution using the Barrett–Joyner–Halenda (BJH) method, that is, smaller pores in regions of 1 nm to 8 nm and larger pores ranging from 10 nm to 120 nm. Indeed, the formation of hierarchical nanopore structures on a multi-length scale was highly conducive to lithium ion insertion and extraction reactions, as well as the electrolyte transportation. However, the nanorods obtained at 500 °C just showed a small hysteresis loop with flat and low single-modal pore-size distribution curve. As T_d increased, the pore peak located at the small mesopore region shifted gradually to the larger mesopore region and disappeared at 500 °C; the one located at the large mesopore region strengthened first and then weakened. These variations accorded with the structure evolution of the products.

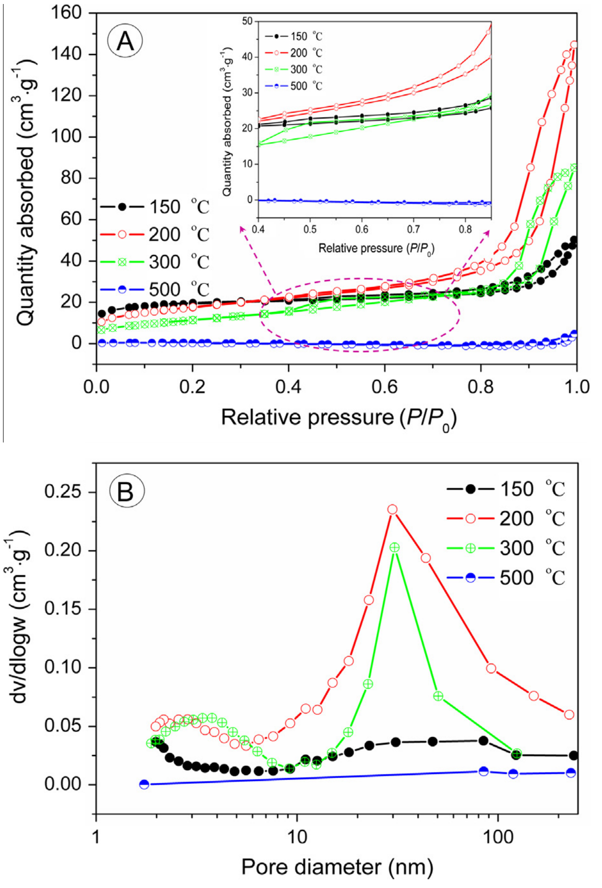

Fig. 6. Nitrogen adsorption/desorption isotherms (A) and the corresponding pore size distribution curves (B) of the products obtained at various T_d.

The details about the specific surface area (S_{BET}), pore volume (V), and pore size (D) of the samples derived from the nitrogen adsorption/desorption isotherm are listed in Table 1. These data clearly show that the S_{BET} decreased from 66.31 $m^2\,g^{-1}$ to 0.65 $m^2\,g^{-1}$ with T_d increasing from 150 °C to 500 °C, whereas V and D showed the reversed U-shape variations. The S_{BET} values of 66.31 $m^2\,g^{-1}$ for nanobowls and 63.01 $m^2\,g^{-1}$ for nanotube arrays were significantly larger than 24.8 $m^2\,g^{-1}$ of macroporous Co_3O_4 platelets and 7.6 $m^2\,g^{-1}$ of nanotubes [23]. A possible reason is that T_d provided different driving forces for the growth of nanocrystals and the mass transport rate of the gas bubbles. At low T_d, the growth and nucleation rates of nuclei were small, but the increased mass transport rate of the gas with T_d facilitated the enlargement of pore volume and pore size. Therefore, the high growth and nucleation rates of nuclei at relatively high T_d are the key factors for the formation of the solid structures. Similar phenomenon can also be reported in our previous work [48,49].

3.5. Electrochemical properties

The electrochemical performance of as-prepared Co_3O_4 samples was evaluated by a standard method based on Co_3O_4/Li haft cell, in which Co_3O_4 and lithium foil worked as positive and negative electrode, respectively. Fig. 7A shows the voltage/capacity curves for the Co_3O_4 nanobowls/Li cell, measured between 3.00 and 0.01 V, which was similar to those of Co_3O_4 nanomaterials with other structures prepared by other methods. During the first discharge, the voltage decreased steeply to approximately 1.0 V, whereupon a plateau set in and continued until a capacity of approximately 1000 mA g^{-1}, followed by a gradual drop in voltage until the end of discharge. As for the Co_3O_4 nanobowl arrays, only one well-defined voltage plateau at approximately 1.0 V was observed, which is generally attributed to the reduction processes from Co^{3+} to Co^0 [23] No high voltage plateau was observed at ca. 1.3 eV, which was previously caused by low surface area or very low current density of nanotextured Co_3O_4. According to the reaction mechanism proposed in the earlier studies [15,21,38], the following chemical reactions were involved in the discharging and charging process.

$$Co_3O_4 + 8Li + 8e^- \leftrightarrow 4Li_2O + 3Co^0 \tag{2}$$

$$8Li \leftrightarrow 8Li^+ + 8e^- \tag{3}$$

$$Co_3O_4 + 8Li \underset{\text{charge}}{\overset{\text{discharge}}{\rightleftarrows}} 4Li_2O + 3Co^0 \tag{4}$$

Fig. 7B shows the curves of specific capacities versus cycle number for the Co_3O_4 nanobowl electrodes at various current densities. The Co_3O_4 nanobowl electrodes had an initial discharge capacity

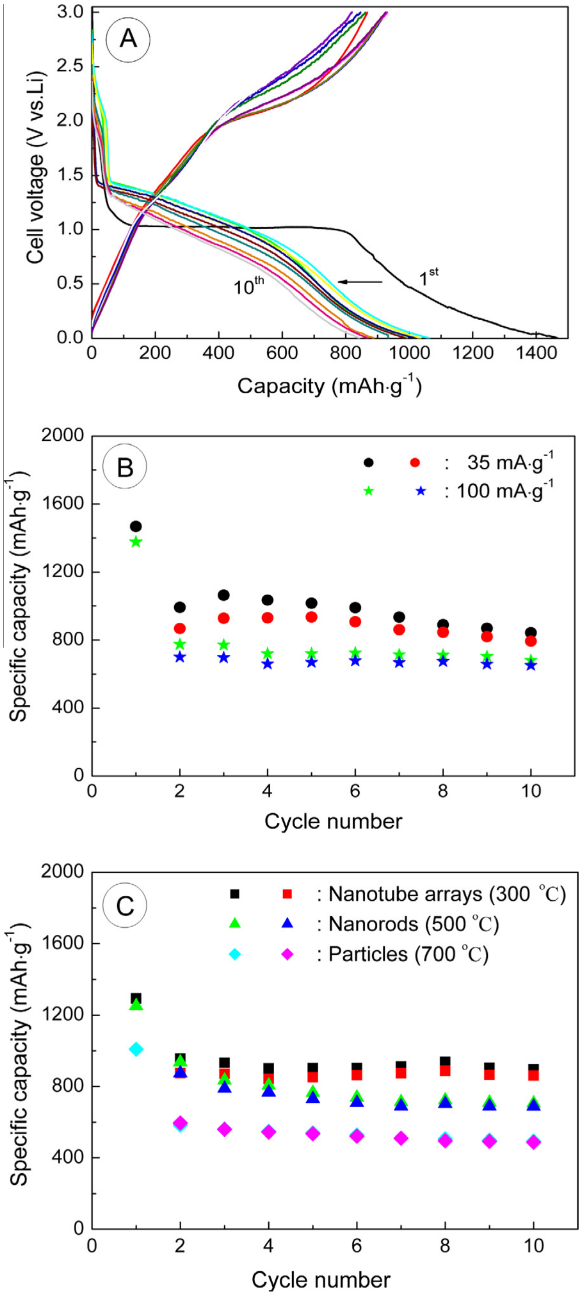

Fig. 7. (A) Discharging and charging curves of the electrodes made by the as-prepared Co_3O_4 nanobowl arrays obtained at 150 °C cycled between 3.00 and 0.01 V at 35 mA g^{-1} and 20 °C. Specific capacities versus cycle number for the electrodes made by (B) Co_3O_4 nanobowl arrays and (C) other Co_3O_4 nanostructures obtained at different temperatures of 300 °C to 700 °C at 35 mA g^{-1}. For each set of data, the upper dot is for discharge and the lower dot is for charge.

as high as 1467.9 mAh g^{-1} at the current density of 35 mA g^{-1} and 1376.8 mAh g^{-1} at the current density of 100 mA g^{-1}. The above values are larger than their theoretical values (890 mAh g^{-1}), owing to irreversible reactions (e.g., decomposition of electrolyte) to form a solid electrolyte interphase layer or possibly interfacial lithium storage [50,51]. Note that the capacities were higher than those of Co_3O_4 nanoparticles (830 mAh g^{-1}), nanobelts (1204 mAh g^{-1}) [52], Co_3O_4 nanotubes (850 mAh g^{-1}) [53], and mesoporous nanowire arrays (1124 mAh g^{-1}) [20].

Just as many electrode materials, Co_3O_4 nanobowl arrays displayed a large irreversible loss of 26–30% in the first cycle. This inevitable loss is normally ascribed to agglomeration [54], growth of passivation layers [55], electrolyte degradation, dissolution of the active material within the organic electrolyte occurring during first discharge [50], or concomitant formation of the decomposition layer on the surface of the reduced particles [56]. However, these nanobowl arrays still maintained a capacity as high as 992.3 mAh g^{-1} at 35 mA g^{-1} and 774.8 mAh g^{-1} at 100 mA g^{-1} after the first cycle. Moreover, these high capacities could almost be completely retained even after 10 cycles (Fig. 7B) with 843.2 mAh g^{-1} at 35 mA g^{-1} and 680.1 mAh g^{-1} at 100 mA g^{-1}, corresponding to a fading rate of 0.6% per cycle. Additionally, 843.2 mAh g^{-1} was higher than that (750 mAh g^{-1}) of nanowires and that (ca. 800 mAh g^{-1}) of mesoporous nanowire arrays [20].

To further reveal the effect of morphology and structure on electrochemical properties, the electrochemical performance of polymorphous Co_3O_4 samples were also investigated under the same conditions (Fig. 7C). The initial discharge capacities of nanotube array, nanorods, and microspheres were 1293.05, 1250.77, and 1008.62 mAh g^{-1} at 35 mA g^{-1}, respectively. After the first cycle, the above initial capacities decreased by 73.87% to 955.19 mAh g^{-1} for nanotube arrays, 74.86% to 936.28 mAh g^{-1} for nanorods, and by 57.80% to 582.98 mAh g^{-1} for microspheres. After 10 cycles, Co_3O_4 nanotube arrays still took on a high capacity of 895.2 mAh g^{-1}, whereas nanorods and microspheres only showed charge capacities of 709.8 mAh g^{-1} and 538.2 mAh g^{-1}, respectively.

The data clearly indicate that nanobowl and nanotube arrays formed at low T_d exhibited higher capacities and better cyclic life than those solid products obtained at the high T_d. The superior electrochemical performances were caused by the aforesaid nanoscaled materials with low crystallization, small grain size, high S_{BET}, hierarchically porous structure, and orderly arrangements. First, quantum and surface effects from nanobowls and nanotubes formed at low T_d strongly affected electrochemical activities. As we know, nanomaterials have more exposed high-energy crystal planes and dangling bonds on the surface, which reduce the oxidation–reduction gaps and enhance chemical reactivity, causing the acceleration of reaction rates. In the current study, the lower T_d helps the formation of the products with smaller grain size and lower crystallization (see Table 1). In this case, with decreased T_d, an increasing proportion of the total number of atoms lay on the surface, improving the structural strains and being more active for lithium electrochemical reaction. This event led to the capacity ordered as Co_3O_4 nanobowl arrays > Co_3O_4 nanotube arrays > Co_3O_4 nanorods > Co_3O_4 microspheres. Second, large specific surface areas of bowl-shaped/tube-like hollow structures provided more grain boundaries for lithium insertion and facilitated the delivery of lithium ions and electrons to the surface and therefore provided more active sites. Third, the hierarchically porous structures could enhance the contact area between the electrode and electrolyte, shorten diffusion length for lithium ions, allow better penetration of the electrolyte, and accommodate the large volume changes induced by lithium insertion/extraction, thereby enhancing the rate cycling stability [57].

The structures suffer from poor capacity retention upon cycling and/or poor rate capability, which remains the major challenge for use in practical cells. However, still nearly 100% capacity retention may be obtained by using additive or prelithiation for compensation or the active modification of the tubular wall [48,58,59]. Thus, the Co_3O_4 nanobowl and nanotube arrays will be under consideration as electrode materials or advanced lithium batteries in the future.

4. Conclusions

In summary, Co_3O_4 nanobowl arrays, nanotube arrays, nanorods, and microspheres have been successfully synthesized via a simple, one-pot template-free method. The morphological evolution was ascribed to the gas bubbles in situ generated in the decompounding reaction of $Co(NO_3)_2{\cdot}6H_2O$, which can direct the self assembly of Co_3O_4 nuclei by tuning only the T_d. The study of electrochemical properties revealed that Co_3O_4 nanobowl and nanotube arrays formed at the low T_d possessed excellent electrochemical cycling properties and higher capacity than nanorods and microspheres formed at the high T_d. The approach presented here for the synthesis of the nanobowl and nanotube arrays can possess such advantages as low cost, convenience, and high efficiency, which can overcome the disadvantages of template methods. Continuing research of applying the gas bubble assisted assembly technique to other nanostructures will be focused on further understanding and controlling the self-assembly behavior of nanomaterials with the aid of the gas bubbles. As a result of low crystallization, small grain size, high S_{BET}, hierarchically porous structure, and orderly arrangements revealed in the Co_3O_4 samples, these nanostructured oxides might be advantageous for chemical sensing, magnetic shielding, luminescence, catalysis, energy storage, controlled release, and cellular applications.

Acknowledgements

This work is financially supported by the National Natural Scientific Foundation of China (51102215), Chinese Scholarship Council (201208330114), Natural Scientific Foundation of Zhejiang Province (Y4100022), Teacher Training Project of Zhejiang Normal University (KYJ06Y12134), and National Innovation and Entrepreneurship Training Program of Undergraduates (201310345016).

References

[1] A.K. Srivastava, S. Madhavi, T.J. White, R.V. Ramanujan, J. Mater. Chem. 15 (2005) 4424–4428.
[2] X. Wang, E. Graugnard, J.S. King, Z. Wang, C.J. Summers, Nano Lett. 4 (2004) 2223–2226.
[3] T. Ito, S. Okazaki, Nature 406 (2000) 1027–1031.
[4] J. Peng, X. Li, D.H. Kim, W. Knoll, Macromol. Raid Commun. 28 (2007) 2055–2061.
[5] J.Y. Chen, D.M. Chao, X.F. Lu, W.J. Zhang, S.K. Manohar, Macromol. Rapid Commun. 27 (2006) 771–775.
[6] Y.F. Wang, J.H. Zhang, X.L. Chen, X. Li, Z.Q. Sun, K. Zhang, D.Y. Wang, B. Yang, J. Colloid Interface Sci. 322 (2008) 327–332.
[7] X.D. Wang, C.S. Lao, E. Graugnard, C.J. Summers, Z.L. Wang, Nano Lett. 5 (2005) 1784–1788.
[8] T. Yu, B. Varghese, Z. Shen, C.T. Lim, C.H. Sow, Mater. Lett. 62 (2008) 389–393.
[9] J.B. Liu, M.G. Zhu, P. Zhan, H. Dong, Y.E. Dong, X.T. Qu, Y.H. Nie, Z.L. Wang, Nanotechnology 17 (2006) 4191–4194.
[10] X. Chen, X. Wei, K. Jiang, Opt. Express 16 (2008) 11888–11893.
[11] J. Ye, P.V. Dorpe, W.V. Roy, G. Borghs, G. Maes, Langmuir 25 (2009) 1822–1827.
[12] S. Farhadi, J. Safabakhsh, J. Alloys Comp. 515 (2012) 180–185.
[13] K.G. Chandrappa, T.V. Venkatesha, J. Alloys Comp. 542 (2012) 68–77.
[14] P.B. Liu, Y. Huang, L. Wang, W. Zhang, J. Alloys Comp. 573 (2013) 151–156.
[15] C. Yu, K. Yang, J.C. Yu, F. Cao, X. Li, X. Zhou, J. Alloys Comp. 509 (2011) 4547–4552.
[16] R. Xu, H.C. Zeng, J. Phys. Chem. B 107 (2003) 926–930.
[17] C.H. Chen, S.F. Abbas, A. Morey, S. Sithambaram, L.P. Xu, H.F. Garces, W.A. Hines, S.L. Suib, Adv. Mater. 20 (2008) 1205–1209.
[18] L. Li, Y. Li, S. Gao, N. Koshizaki, J. Mater. Chem. 19 (2009) 8366–8371.
[19] (a) K.T. Nam, D.W. Kim, P.J. Yoo, C.Y. Chiang, N. Meethong, P.T. Hammond, Y.M. Chiang, A.M. Belcher, Science 312 (2006) 885–888.
[20] X. Yao, X. Xin, Y. Zhang, J. Wang, Z. Liu, X. Xu, J. Alloys Comp. 521 (2012) 95–100.
[21] X.W. Lou, D. Deng, J.Y. Lee, J. Feng, L.A. Archer, Adv. Mater. 20 (2008) 258–262.
[22] N. Du, H. Zhang, B.D. Chen, J.B. Wu, X.Y. Ma, Z.H. Liu, Y.Q. Zhang, D.R. Yang, X.H. Huang, J.P. Tu, Adv. Mater. 19 (2007) 4505–4509.
[23] T. Yu, Y.W. Zhu, X.J. Xu, Z.X. Shen, P. Chen, C.T. Lim, J.T.L. Thong, C.H. Sow, Adv. Mater. 17 (2005) 1595–1599.
[24] M. Liao, Y. Liu, Z. Hu, Q. Yu, J. Alloys Comp. 562 (2013) 106–110.
[25] S.S. Kumari, U.T.S. Pillai, B.C. Pai, J. Alloys Comp. 509 (2011) 2503–2509.
[26] H.Y. Lin, J.D. Wei, C.C. Ou, J.W. Lu, C.Y. Tsai, J. Alloys Comp. 509 (2011) 7009–7015.
[27] Y. Liang, P. Wang, H.B. Dai, J. Alloys Comp. 491 (2010) 359–365.
[28] L.T. Qu, G.Q. Shi, F.E. Chen, J.X. Zhang, Macromolecules 36 (2003) 1063–1067.
[29] L.T. Qu, G.Q. Shi, J.Y. Yuan, G.Y. Han, F.E. Chen, J. Electroanalytical Chem. 561 (2004) 149–156.
[30] Y.Y. Gao, L. Zhao, H. Bai, Q. Chen, G.Q. Shi, J. Electroanalytical Chem. 597 (2006) 13–18.
[31] V. Baipai, P. He, L. Dai, Adv. Funct. Mater. 14 (2004) 145–151.
[32] M. Mazur, J. Phys. Chem. C 112 (2008) 13528–13534.
[33] L. Guo, F. Liang, X.G. Wen, S.H. Yang, L. He, W.Z. Zheng, C.P. Chen, Q.P. Zhong, Adv. Funct. Mater. 17 (2007) 425–430.
[34] S.M. Yoon, H.C. Choi, Current Appl. Phys. 6 (2006) 747–751.
[35] G.X. Tong, J.G. Guan, X.A. Fan, W. Wang, F.H. Song, Chinese J. Inorg. Chem. 24 (2008) 270–274.
[36] G.X. Tong, J.G. Guan, Z.D. Xiao, F.Z. Mou, W. Wang, G.Q. Yan, Chem. Mater. 20 (2008) 3535–3539.
[37] G.X. Tong, J.G. Guan, Z.D. Xiao, X. Huang, Y. Guan, J. Nanopart. Res. 12 (2010) 3025–3037.
[38] G.X. Tong, J.G. Guan, Q.J. Zhang, Adv. Funct. Mater. 23 (2013) 2405–2413.
[39] C. Diekinson, W.Z. Zhou, R.P. Hodgkins, Y.F. Shi, D.Y. Zhao, H.Y. He, Chem. Mater. 18 (2006) 3088–3095.
[40] T. He, D.R. Chen, X.L. Jiao, Y.L. Wang, Y.Z. Duan, Chem. Mater. 17 (2005) 4023–4030.
[41] J.A. Gaddsden, Infrared spectra of minerals and related inorganic compounds, Butterworth, London, 1975. p 44.
[42] Z.P. Xu, H.C. Zeng, Chem. Mater. 12 (2000) 3459–3465.
[43] G.X. Tong, J.G. Guan, Q.J. Zhang, Mater. Chem. Phys. 127 (2011) 371–378.
[44] K. Nakamoto, (Trans: D. Huang, R.Wang) Infrared spectra of inorganic and coordination compound, 4th Chemical Industry Press, Beijing, 1991. p 251.
[45] Y.G. Li, B. Tan, Y.Y. Wu, J. Am. Chem. Soc. 128 (2006) 14258–14259.
[46] E. Fouissac, M. Milas, M. Rinaudo, Macromolecules 26 (1993) 6945–6951.
[47] J. Kestin, H.E. Khalifa, R.J. Correia, J. Phys. Chem. Ref. Data 10 (1981) 71–87.
[48] G.X. Tong, F.F. Du, L.J. Xiang, F.T. Liu, L.L. Mao, J.G. Guan, Nanoscale 6 (2014) 778–787.
[49] G.X. Tong, F.F. Du, W.H. Wu, R.N. Wu, F.T. Liu, Y. Liang, J. Mater. Chem. B 1 (2013) 2647–2657.
[50] G. Binotto, D. Larcher, A.S. Prakash, R.H. Urbina, M.S. Hegde, J.M. Tarascon, Chem. Mater. 19 (2007) 3032–3040.
[51] S. Laruelle, S. Grugeon, P. Poizot, M. Dolle, L. Dupont, J.M. Tarascon, J. Electrochem. Soc. 149 (2002) A627–A634.
[52] H. Huang, W.J. Zhu, X.Y. Tao, Y. Xia, Z.Y. Yu, J.W. Fang, Y.P. Gan, W.K. Zhang, ACS Appl. Mater. Inter. 4 (2012) 5974–5980.
[53] W.Y. Li, L.N. Xu, J. Chen, Adv. Funct. Mater. 15 (2005) 851–857.
[54] I.A. Courtney, W.R. McKinnon, J.R. Dahn, J. Electrochem. Soc. 146 (1999) 59–68.
[55] S. Denis, E. Baudrin, M. Touboul, J.M. Tarascon, J. Electrochem. Soc. 144 (1997) 4099–4109.
[56] P. Poizot, S. Laruelle, S. Grugeon, L. Dupont, J.M. Tarascon, Nature 407 (2000) 496–499.
[57] G.X. Tong, J.G. Guan, W.H. Wu, L.C. Li, Y. Guan, Q. Hua, Sci. China Technol. Sci. 53 (2010) 1897–1903.
[58] M.S. Park, G.X. Wang, Y.M. Kang, D. Wexler, S.X. Dou, H.K. Liu, Angew. Chem. Int. Ed. 46 (2007) 750–753.
[59] Y. Wang, H.C. Zeng, J.Y. Lee, Adv. Mater. 18 (2006) 645–649.